

ECINADS-D6.2b: The impact of dynamic and variational multiscale LES modelling in hybrid calculations, march 2012.

Stephen Wornom^a, Carine Moussaed^b, Anca Belme^c,
Maria-Vittoria Salvetti^d, Bruno Koobus^b, Alain Dervieux^c

^a LEMMA, 2000 Route des Lucioles, 06902 Sophia-Antipolis, France

^b Département de Mathématiques, Université Montpellier 2,
Place Eugène Bataillon, 34095 Montpellier cedex, France

^c INRIA, 2004 Route des Lucioles, 06902 Sophia-Antipolis, France

^d Dipartimento di Ingegneria Aerospaziale, Università di Pisa, Via G. Caruso 8, 56122 Pisa (Italy)

Abstract

We study the impact of the introduction of dynamic LES modeling and VMS-LES in the high Reynolds flow around a cylinder.

1 Introduction

After the proposition by Spalart and co-workers for combining RANS modeling and LES modeling into hybrid models, the use of LES models have shown an important expansion in industrial simulations. In the DES model, a RANS model, the Spalart-Allmaras one-equation model, is blended with its adaptation to LES by the introduction of mesh size in the source term of the turbulent viscosity. In the LES zone, therefore, a one equation LES model of Boussinesq type applies.

Of course, the main difficulty in doing this hybridization comes from the strong difference between the flow variable of RANS, a statistical mean, and the flow variable of LES, obtained from a low-pass filtering of the complete flow. In particular, keeping a good predictivity when passing from a zone where RANS is applied to a zone where LES is applied is an important challenge which have motivated many studies (Spalart, Goldberg). This paper does not address this issue.

Once in the LES zone, the prediction quality will depend on the quality of the LES model. In the present work, we are interested by the non expensive computation of high Reynolds blunt body flows and examine the impact of the basic choices in the LES component.

LES asymptotic convergence: any LES model is theoretically able to produce a good prediction of the flow under study as soon as the mesh is fine enough. This is true, in theory, for the basic Smagorinsky model, but in practice, convergence does not applies for realistic meshes, due to the too large viscosity near a wall. In this paper we concentrate on the options allowing to predict rather accurately for a mesh as coarse as possible:

LES practical convergence: for a given prediction accuracy, a LES model giving the same accuracy for a coarser mesh than another LES model is of better practical convergence. In particular, we shall consider two modelling methods which proved to bring a better practical convergence. On one side, the dynamic method of [20] allows to adapt the filter size in spatial direction. The dynamic method transforms a bad LES model for boundary layers into a good one. It shows improvement in complex flows as for example drag crisis flow around a cylinder [2]. On the other side, the Variational Multiscale (VMS) formulation of [13] allows to adapt the filter size according to spatial scale. It permits to reduce the spurious damping of large scales and therefore to get closer to a correct backscatter process. From this standpoint, it can be considered as having a complementary action with respect to Dynamic modeling. It also transforms a bad LES model for boundary layers into a good one. It also shows improvement for shear layers [33].

The purpose of this paper is to examine the improvements carried by VMS and dynamic modeling when used separately or in combination inside a hybrid model. Our benchmark is a Reynolds interval of supercritical flows past a circular cylinder. The interval between $Rey=0.5$ million and $Rey=8$ millions corresponds to a large set of industrial applications, from aeronautics to off shore. This interval covers the supercritical, high transition, and transcritical regimes according to Sumer and Fredsoe [32]. The $Rey=0.5$ million corresponds to a supercritical regime just after the drag crisis arising around $Rey=0.3$ million, the drag is about locally minimal, and the drag-to-Reynolds variation is rather small. Then an important drag recovery is observed when the Reynolds number is further increased. The $Rey=8$ millions regime corresponds again to a slow variation of the drag. Measurements of these flows involve the well known drag curve of ..., and [31, 30, 35] Although being the minimal output of this kind of simulation, The prediction of the drag level is a rather difficult task. These flows are generally computed with RANS modeling, we refer to [7] A few attempts have been done with LES models, see [36, 6]. DES calculations are also done in [5]. Beside drag level, the prediction of Reynolds effect, with quasi stagnation of drag, then increase of it and at last quasi stagnation again is also a challenge. Calculations with several different Reynolds numbers are, at our knowledge, not so many, see however [8]

2 Variational Multiscale LES approach

The VMS formulation consist in splitting between the large resolved scales (LRS) i.e. those resolved on a virtual coarser grid, and the small resolved ones (SRS). The VMS-LES method does not compute the SGS component of the solution, but modelizes its effect on the small resolved scales which corresponds to the highest level of discretization, and preserves the Navier-Stokes model for the large resolved scales.

2.1 VMS formulation

In the present work, we adopt the VMS approach proposed by Koobus and Farhat [16] for the simulation of compressible turbulent flows through a finite volume/finite element discretization on unstructured tetrahedral grids. Let V_{FV} be the space spanned by Φ_k , the finite volume basis function and V_{FE} the one spanned by ψ_k , the finite element basis function. In order to separate coarse- and fine- scales, these spaces are decomposed as: $\psi_k = \overline{\psi}_k + \psi'_k$ and $\phi_k = \overline{\phi}_k + \phi'_k$ where overline denotes a coarse scale and the prime a fine scale. Consequently to this decomposition, the variables of the flow are decomposed as follows:

$$W = \overline{W} + W' + W^{SGS} \quad (1)$$

where \overline{W} are the LRS, W' the SRS and W^{SGS} are the unresolved scales. In [16], a projector operator based on spatial average on macro-celles is defined in the LRS space to determinate the basis functions of the LRS space:

$$\overline{\psi}_k = \frac{Vol(C_k)}{\sum_{j \in I_k} Vol(C_j)} \sum_{j \in I_k} \psi_j \quad (2)$$

for finite volumes, and

$$\overline{\phi}_k = \frac{Vol(C_k)}{\sum_{j \in I_k} Vol(C_j)} \sum_{j \in I_k} \phi_j \quad (3)$$

for finite elements. $Vol(C_j)$ designate the volume of C_j , the cell around the vertex j . $I_k = j/C_j \in C_{m(k)}$ and $C_{m(k)}$ denotes the macro-cell containing the cell C_k . The macro-celles are obtained by a process known as agglomeration [22]. The SGS model which modelizes the dissipatif effect of the unresolved scales on the resolved scales is only added to the fine-resolved scales. The term bellow is added to the fine-scale momentum equation

$$\int_{\Omega} \tau' \nabla \Phi' d\Omega \quad (4)$$

Where $\tau'_{ij} = -\mu'_t(2S'_{ij} - \frac{2}{3}S'_{kk}\delta_{ij})$ and $S'_{ij} = \frac{1}{2}(\frac{\partial u'_i}{\partial x_j} + \frac{\partial u'_j}{\partial x_i})$ and μ'_t designate the viscosity of the SGS model used to close the problem. Likewise, the term

$$\int_{\Omega} \frac{C_p \mu'_t}{Pr_{sgs}} \nabla T' \cdot \nabla \Phi' d\Omega \quad (5)$$

is added to the fine scales energy equation. C_p is the specific heat at constant pressure and Pr_t is the subgrid-scale Prandtl number which is assumed to be constant.

2.2 SGS viscosities

Smagorinsky

To approximate the SGS Reynolds stress a SGS model can be employed. The most commonly used SGS models in LES is the Smagorinsky model in which the eddy viscosity is defined by

$$\mu_{sgs} = \bar{\rho} (C_s \Delta)^2 |\tilde{S}| \quad , \quad (6)$$

where Δ is the filter width, C_s is the Smagorinsky coefficient and $|\tilde{S}| = \sqrt{2\tilde{S}_{ij}}$. A typical value for the Smagorinsky coefficient is $C_s = 0,1$ that is often used, especially in the presence of the mean shear.

WALE

The second SGS model we considered is the Wall-Adapting Local Eddy -Viscosity (WALE) SGS model proposed by Nicoud and Ducros [23]. The eddy-viscosity term μ_{sgs} of the model is defined by:

$$\mu_{sgs} = \bar{\rho} (C_w \Delta)^2 \frac{(\tilde{S}_{ij}^d \tilde{S}_{ij}^d)^{\frac{3}{2}}}{(\tilde{S}_{ij} \tilde{S}_{ij})^{\frac{5}{2}} + (\tilde{S}_{ij}^d \tilde{S}_{ij}^d)^{\frac{5}{4}}} \quad (7)$$

with being the symmetric part of the tensor $g_{ij}^2 = g_{ik}g_{kj}$, where $g_{ij} = \partial \tilde{u}_i / \partial x_j$:

$$\tilde{S}_{ij}^d = \frac{1}{2}(g_{ij}^2 + g_{ji}^2) - \frac{1}{3}\delta_{ij}g_{kk}^2$$

2.3 Dynamic model

Historically, the constant (C_s, C_w) appearing in the expression of the viscosity of a SGS model was often arbitrarily set to a constant over entire flow field. For general inhomogeneous flows, it can be a strong function of space. This constant is replaced, according to Germano et al. [20], with a dimensionless parameter $C(x, t)$ that is allowed to be a function of space and time. This dynamic procedure provides a systematic way of adjusting C_s or C_w allowing it to be a function of position which is desirable for inhomogeneous flows. A novel feature of this method is that $C(x, t)$ is estimated dynamically using information from the resolved scales making the model self-tuning. The so-called dynamic model [20] has been refined [28, 19] over the past several years and has been successfully used to study a variety of complex inhomogeneous flows. The first step in the dynamic model consists in the introduction of a second filter, larger than the filter width, which is called the test-filter. The test-filter is applied to the grid filtered Navier Stokes equations, then, the sub test-scale stress is defined as

$$M_{ij}^{test} = \widehat{\rho \mathbf{u}_i \mathbf{u}_j} - (\hat{\rho})^{-1} \left(\widehat{\rho \mathbf{u}_i} \widehat{\rho \mathbf{u}_j} \right) \quad (8)$$

and, can be written using a Smagorinsky or WALE model, as

$$M_{ij}^{test} - \frac{1}{3} M_{kk}^{test} \delta_{ij} = -C \hat{\Delta}^2 \hat{\rho} g(\hat{\mathbf{u}}) \hat{P}_{ij} \quad (C \text{ denotes } C_w^2 \text{ or } C_s^2) \quad (9)$$

We recall that the over-line denotes the grid filter, the tilde the Favre filter and the chapeau the test-filter, and C , as originally shown by Germano et al. [20], is chosen so that the subgrid-scale is consistent with the subtest-scale. The quantity

$$\mathcal{L}_{ij} = M_{ij}^{test} - \hat{M}_{ij} = \widehat{\tilde{\rho} \mathbf{u}_i \tilde{\mathbf{u}}_j} - (\hat{\tilde{\rho}})^{-1} \left(\widehat{\tilde{\rho} \mathbf{u}_i} \widehat{\tilde{\rho} \mathbf{u}_j} \right) \quad (10)$$

is called the Leonard stress. In order to determine the constant, one can compare L_{ij} to the value that would be obtained using the SGS model (Smagorinsky or WALE). This leads to

$$L_{ij} = \mathcal{L}_{ij} - \frac{1}{3}\mathcal{L}_{kk}\delta_{ij} = (C\Delta^2)B_{ij} \quad (11)$$

where

$$B_{ij} = \widehat{\bar{\rho}g(\hat{\mathbf{u}})\hat{P}_{ij}} - \left(\frac{\hat{\Delta}}{\Delta}\right)^2 \hat{\rho}g(\hat{\mathbf{u}})\hat{P}_{ij}$$

Equation (11) represents six equations with one unknown. The unknown $(C\Delta^2)$ has to satisfy

$$L_{ij} = (C\Delta^2)B_{ij} \quad (12)$$

This system of six equations can be resolved using the least squares approach. $(C\Delta^2)$ minimizes the quantity

$$Q = (L_{ij} - (C\Delta^2)B_{ij})^2 \quad (13)$$

Thus, $(C\Delta^2)$ is found by setting $\frac{\partial Q}{\partial (C\Delta^2)} = 0$, from which we derive the value of $(C\Delta^2)$:

$$(C\Delta^2) = \frac{L_{ij}B_{ij}}{B_{pq}B_{pq}}. \quad (14)$$

A drawback to the development of any dynamic version based on the Germano-identity [20] could be caused by the sensitivity of SGS models having the correct behavior near the wall to the filtering procedure and the stabilization method. A simple way to avoid this inconvenient is to have a sensor able to detect the presence of the wall, without a priori knowledge of the geometry, so that the considered SGS model of WALE adapts the classical constant of the model, which is equal to 0,5 in the near wall region, and compute the constant dynamically otherwise. We adapt the sensor proposed in [Baya], the expression of which is:

$$SVS = \frac{S_{ij}^d S_{ij}^{d\frac{3}{2}}}{S_{ij}^d S_{ij}^{d\frac{3}{2}} + S_{ij} S_{ij}^3} \quad (15)$$

This parameter has the property to behave like y^{+3} , to be equal to 0 for pure shear flows and 1 for pure rotating flows.

3 Hybrid Model

3.1 Hybrid RANS/LES Coupling

The Navier-Stokes equations for compressible flows of perfect newtonian gases are considered here, in conservative form and using the following variables: density (ρ), momental (ρu_i , $i = 1, 2, 3$) and total energy per unit volume ($E = \rho e + 1/2\rho u_i u_i$, e being the internal energy).

As in [29], the following decomposition of the flow variables is adopted:

$$W = \underbrace{\langle W \rangle}_{RANS} + \underbrace{W^c}_{correction} + W^{SGS}$$

where $\langle W \rangle$ are the RANS flow variables, obtained by applying an averaging operator to the Navier-Stokes equations, W^c are the remaining resolved fluctuations (i.e. $\langle W \rangle + W^c$ are the flow variables in LES) and W^{SGS} are the unresolved or SGS fluctuations.

If we write the Navier-Stokes equations in the following compact conservative form:

$$\frac{\partial W}{\partial t} + \nabla \cdot \mathcal{F}(W) = 0$$

in which \mathcal{F} represents both the viscous and the convective fluxes, for the averaged flow $\langle W \rangle$ we get:

$$\frac{\partial \langle W \rangle}{\partial t} + \nabla \cdot \mathcal{F}(\langle W \rangle) = -\tau^{RANS}(\langle W \rangle) \quad (16)$$

where $\tau^{RANS}(\langle W \rangle)$ is the closure term given by a RANS turbulence model.

As it was previously explained, by applying a filtering operator to the Navier-Stokes equations, the LES equations are obtained, which can be written as follows:

$$\frac{\partial(\langle W \rangle + W^c)}{\partial t} + \nabla \cdot \mathcal{F}(\langle W \rangle + W^c) = -\tau^{LES}(\langle W \rangle + W^c) \quad (17)$$

where τ^{LES} is the SGS term.

An equation for the resolved fluctuations W^c can thus be derived (see also [29]):

$$\begin{aligned} \frac{\partial W^c}{\partial t} + \nabla \cdot \mathcal{F}(\langle W \rangle + W^c) - \nabla \cdot \mathcal{F}(\langle W \rangle) \\ = \tau^{RANS}(\langle W \rangle) - \tau^{LES}(\langle W \rangle + W^c). \end{aligned} \quad (18)$$

The basic idea of the proposed hybrid model is to solve System (16) in the whole domain and to correct the obtained averaged flow by adding the remaining resolved fluctuations (computed through Equation (18)), wherever the grid resolution is adequate for LES. To identify the regions where the additional fluctuations must be computed, we introduce a blending function θ smoothly varying between 0 and 1. When $\theta = 1$, no correction to $\langle W \rangle$ is computed and, thus, the RANS approach is recovered. Conversely, wherever $\theta < 1$, additional resolved fluctuations are computed; in the limit of $\theta \rightarrow 0$ we want to recover a full LES approach. Thus, the following equation is used for the correction term:

$$\begin{aligned} \frac{\partial W^c}{\partial t} + \nabla \cdot \mathcal{F}(\langle W \rangle + W^c) - \nabla \cdot \mathcal{F}(\langle W \rangle) \\ = (1 - \theta) \left[\tau^{RANS}(\langle W \rangle) - \tau^{LES}(\langle W \rangle + W^c) \right]. \end{aligned} \quad (19)$$

Note that for $\theta \rightarrow 0$ the RANS limit is actually recovered; indeed, for $\theta = 1$ the right-hand side of System (19) vanishes and, hence, a trivial solution is $W^c = 0$. As required, for $\theta = 0$ System (19) becomes identical to System (18) and the remaining resolved fluctuations are added to the averaged flow; the model, thus, works in LES mode. For θ going from 1 to 0, i.e. when, following the definition of the blending function (cf. Relation 36), the grid resolution is intermediate between one adequate for RANS and one adequate for LES, the right-hand side term in Equation (19) is damped through multiplication by $(1 - \theta)$. Although, this seems rather arbitrary from a physical point of view, this is aimed to obtain a smooth transition between RANS and LES. More specifically, we wish to obtain a progressive addition of fluctuations when the grid resolution increases and the model switches from the RANS to the LES mode. Summarizing, the ingredients of the proposed approach are: a RANS closure model, a SGS model for LES and the definition of the blending function. These will be described in Sections 3.2 and ??.

3.2 RANS

Concerning the RANS closure model, the standard $k - \epsilon$ model [17] is used. The main ingredients of this closure model are presented next.

Standard $k - \epsilon$ model. This is an eddy viscosity model with a turbulent viscosity μ_t defined from two extra variables (two-equation model) the turbulent kinetic energy k and its dissipation rate ϵ , and given by expression (??). The Reynolds tensor, the main term to model, is then given by Equation (??).

The k and ϵ fields are evaluated by solving the two extra transport equations:

$$\frac{\partial \langle \rho \rangle k}{\partial t} + \langle \langle \rho \rangle \tilde{u}_j k \rangle_{,j} = \left[\left(\mu + \frac{\mu_t}{\sigma_k} \right) \frac{\partial k}{\partial x_j} \right]_{,j} + R_{ij} \frac{\partial \tilde{u}_i}{\partial x_j} - \langle \rho \rangle \varepsilon \quad , \quad (20)$$

$$\frac{\partial \langle \rho \rangle \varepsilon}{\partial t} + \langle \langle \rho \rangle \varepsilon \tilde{u}_j \rangle_{,j} = \left[\left(\mu + \frac{\mu_t}{\sigma_\varepsilon} \right) \frac{\partial \varepsilon}{\partial x_j} \right]_{,j} + C_{\varepsilon 1} \left(\frac{\varepsilon}{k} \right) R_{ij} \frac{\partial \tilde{u}_i}{\partial x_j} - C_{\varepsilon 2} \langle \rho \rangle \frac{\varepsilon^2}{k} \quad . \quad (21)$$

where constants $C_{\varepsilon 1}$, $C_{\varepsilon 2}$, σ_k and σ_ε are defined by:

$$C_{\varepsilon 1} = 1.44 \quad C_{\varepsilon 2} = 1.92 \quad \sigma_k = 1.0 \quad \sigma_\varepsilon = 1.3$$

Historically these constants are deduced from the application of the model to simple turbulent flows. They also can be mathematically derived by the Renormalization Group method, see [38].

Wall treatment by wall law. The k and ε variables, the velocity and the temperature can have stiff behavior and exhibit small scales near a wall. However, their behavior presents in many case some common features, such as obeying the logarithmic law for the tangent velocity component. In the theory and in the $k - \varepsilon$ formulation, this is a consequence of the equilibrium between turbulent kinetic energy production and dissipation, which arises in a large enough region close to wall. Wall law methods use this feature in order to avoid the costly discretization of the wall behavior of these variables. Closer to the wall, two different behaviors need to be taken into account: in the sublayer and in the *log* region. This is well modeled in Reichardt's law (see for example [12]) which writes in terms of U^+ and y^+ :

$$U^+ = \frac{\bar{U}}{U_\tau} \quad , \quad (22)$$

$$y^+ = \frac{\rho U_\tau}{\mu} y \quad . \quad (23)$$

where \bar{U} is the statistical average of the velocity and the friction velocity U_τ is given by:

$$U_\tau = \sqrt{\frac{\tau_p}{\rho}} \quad . \quad (24)$$

Then we set:

$$U^+ = \frac{1}{\kappa} \ln(1 + \kappa y^+) + 7.8 \left(1 - e^{-\frac{y^+}{11}} - \frac{y^+}{11} e^{-0.33 y^+} \right) \quad . \quad (25)$$

where $\kappa = 0.41$ is the von Kàrmàn constant.

In practice, the computational domain is restricted to a domain at a distance d to the wall, with $d > \delta$, where δ is prescribed by the user. The part $d < \delta$ of the flow is represented by the law 25 after evaluation of U_τ and matched to the numerical solution in the computational domain. The matching distance δ is fixed by the user in such a way that its normalised counterpart $y_{match}^+ = \delta \cdot u_f / \gamma$ is in the log region, more precisely:

$$30 < y_{match}^+ < 200 \quad (26)$$

An approximative value of δ is chosen by an empirical formula:

$$\delta = 20 \cdot D \cdot y_{match}^+ / Rey \quad (27)$$

where y_{match}^+ is chosen by Relation 26. In practice the y^+ of the matching zone varies more or less in the interval] 10 – 300 [. D is a characteristic of the dimension of the flow. In our examples, D is the diameter of the obstacle.

A Low Reynolds version. While the wall law is efficient for the CPU standpoint, better prediction of close to the wall, and in particular of separation, is obtained by resolving down to the wall, i.e., applying a low Reynolds closure.

The low Reynolds $k - \varepsilon$ model proposed in [10][9] is presented now. Let:

$$\mu_t = C_\mu f_\mu \rho \frac{k^2}{\varepsilon} \quad (28)$$

where the coefficient $C_\mu = 0.09$ and f_μ is a so-called damping function (for damping the effect of model when closer to wall) defined by:

$$f_\mu = \frac{1 - e^{-A_\mu R_t}}{1 - e^{-R_t^{1/2}}} \max(1, \psi^{-1}) \quad (29)$$

with the constant $A_\mu = 0.01$ and $\psi = R_t^{1/2}/C_\tau$. The turbulent Reynolds number :

$$R_t = k^2/(\nu\varepsilon) \quad \text{with} \quad \nu = \mu/\rho \quad (30)$$

allows us to avoid the estimation of the distance to the wall.

Then, k and ε are solutions of:

$$\frac{\partial \langle \rho \rangle k}{\partial t} + (\langle \rho \rangle \tilde{u}_j k)_{,j} = \left[\left(\mu + \frac{\mu_t}{\sigma_k} \right) \frac{\partial k}{\partial x_j} \right]_{,j} + R_{ij} \frac{\partial \tilde{u}_i}{\partial x_j} - \langle \rho \rangle \varepsilon \quad , \quad (31)$$

$$\begin{aligned} \frac{\partial \langle \rho \rangle \varepsilon}{\partial t} + (\langle \rho \rangle \varepsilon \tilde{u}_j)_{,j} &= \left[\left(\mu + \frac{\mu_t}{\sigma_\varepsilon} \right) \frac{\partial \varepsilon}{\partial x_j} \right]_{,j} + \\ &\left(C_{\varepsilon 1} R_{ij} \frac{\partial \tilde{u}_i}{\partial x_j} - C_{\varepsilon 2} \langle \rho \rangle \varepsilon + E \right) T_\tau^{-1} \quad . \end{aligned} \quad (32)$$

where T_τ is the realizable time scale:

$$T_\tau = \frac{k}{\varepsilon} \max(1, \psi^{-1}). \quad (33)$$

This time scale is k/ε for large values of turbulent Reynolds number R_t and thus of ψ , but tends to be equal to the Kolmogorov scale $C_\tau(\nu/\varepsilon)^{1/2}$ for $R_t \ll 1$. Constants are defined as $C_\tau = 1.41$, $C_{\varepsilon 1} = 1.42$, $C_{\varepsilon 2} = 1.83$ and:

$$E = \rho A_E V (\varepsilon T_\tau)^{0.5} \xi \quad (34)$$

with $A_E = 0.3$, $V = \max(\sqrt{k}, (\nu\varepsilon)^{0.25})$ and $\xi = \max(\frac{\partial k}{\partial x_i} \frac{\partial \tau}{\partial x_i}, 0)$, where $\tau = k/\varepsilon$.

In case of very high Reynolds number demanding a very stretched mesh and multiples layers on a small thickness around the obstacle, the matrix of resolution for this low-Reynolds model is bad conditioned and the system difficult to resolve. The main interest of this low-Reynolds model is that it does not need a distance to the wall.

In the sequel we combine this low Reynolds model to the wall law. This is useful because in practice, the approximative empiric choice of the layer length δ does not ensures that small y^+ (smaller than 30) cannot be encountered in some part of the flow. In the case where y^+ is small, the Goldberg model applies and improves the flow prediction.

3.3 Hybrid Complete Formulation

The Galerkin projection of Equations (16) and (17) are hybridized as follows:

$$\begin{aligned} & \left(\frac{\partial W}{\partial t}, \psi_l \right) + (\nabla \cdot F_c(W), \psi_l) + (\nabla \cdot F_v(W), \psi_l) \\ & = -\theta \left(\tau^{RANS}(W), \psi_l \right) - (1 - \theta) \left(\tau^{LES}(W'), \psi_l' \right) \quad l = 1, N \end{aligned} \quad (35)$$

As a possible choice for θ , the following function is used in the present study:

$$\theta = F(\xi) = \tanh(\xi^2) \quad (36)$$

where ξ is the *blending parameter*, which should indicate whether the grid resolution is fine enough to resolve a significant part of the turbulence fluctuations, i.e. to obtain a LES-like simulation. The choice of the *blending parameter* is clearly a key point for the definition of the present hybrid model. In this study, the blending parameter based on ratio length is chosen: $\xi = \frac{\Delta}{l_{RANS}}$ where l_{RANS} is a typical length in the RANS approach i.e. $l_{RANS} = \frac{k^{3/2}}{\epsilon}$, and $\Delta = (Vol(T))^{1/3}$ is representative of the local grid size (T denotes a tetrahedron of the mesh).

Protection zone.

As explained previously, the boundary layer is wished to be treated with RANS model, that is why the definition of the blending function is carefully studied so that no LES computation occurs for massively separated flows when the grid resolution could be misleading. This remark applies to any hybrid model of RANS/LES type. Particularily in our model, similiary to a DDES approach we introduced a *protection zone* by introducing a distance from the wall function denoted *arg*:

$$arg = \frac{10 * l}{|d| + l/1000}. \quad (37)$$

In the expression of *arg* we denoted d the distance to the body surface. l is the thickness parameter, that we defined as 5 times the thickness of the wall law or matching zone δ . This is designed in order to include the boundary layer into the RANS zone of the hybrid formulation. The definition of this zone needs the distance d to the wall and we hope to avoid this in the future, for example by the use of turbulent Reynolds number defined by Relation (30).

Then, the new blending function $\bar{\theta}$ is defined as:

$$\bar{\theta} = \max(\theta, \tanh(arg)). \quad (38)$$

Thus, when $|r - r_{min}| \rightarrow 0$ in (37) then $\bar{\theta} \approx 1$ and when on the contrary $|r - r_{min}| \rightarrow \infty$ then $\bar{\theta} \approx 0$.

4 Numerical discretization

The choice of the numerical discretization will influence in two ways this study. First, we use a numerical scheme for compressible flow which needs to be stabilized by numerical dissipation. As discussed in the Introduction, it is compulsory that the numerical dissipation does not interfere with the LES model. A particular attention is paid to this issue. Second, the VMS formulation is based on the basis functions of the scheme. This issue is addressed in the next section. We recall now the main features of the numerical scheme. Further details can be found in [26] and in [3].

The governing equations are discretized in space using a mixed finite-volume/finite-element method applied to unstructured tetrahedrizations. The adopted scheme is vertex centered, i.e. all degrees of freedom are located at the vertices. P1 Galerkin finite elements are used to discretize the diffusive terms.

A dual finite-volume grid is obtained by building a cell C_i around each vertex i ; the finite-volume cells are built by the rule of medians: the boundaries between cells are made of triangular interface facets. Each of these facets has a mid-edge, a facet centroid, and a tetrahedron centroid as vertices.

The convective fluxes are discretized on this tessellation by a finite-volume approach, i.e. in terms of the fluxes through the common boundaries between each couple of neighboring cells:

$$\sum_{j \in V(i)} \int_{\partial C_{ij}} \mathcal{F}(W, \vec{n}) d\sigma \quad , \quad (39)$$

where $V(i)$ is the set of neighboring nodes to vertex i , ∂C_{ij} is the boundary between cells C_i and C_j , and \vec{n} is the outer normal to the cell C_i and $\mathcal{F}(W, \vec{n})$ the Euler flux in the direction of \vec{n} . The unknowns are discontinuous along the cell boundaries and this allows an approximate Riemann solver to be introduced.

The Roe scheme [24] (with low-Mach preconditioning) represents the basic upwind component for the numerical evaluation of the convective fluxes \mathcal{F} :

$$\int_{\partial C_{ij}} \mathcal{F}(W, \vec{n}) d\sigma \simeq \Phi^R(W_i, W_j, \vec{n}) = \frac{\mathcal{F}(W_i, \vec{n}) + \mathcal{F}(W_j, \vec{n})}{2} - \gamma_s d^R(W_i, W_j, \vec{n}) \quad (40)$$

$$d^R(W_i, W_j, \vec{n}) = P^{-1} |P\mathcal{R}(W_i, W_j, \vec{n})| \frac{W_j - W_i}{2} \quad (41)$$

in which W_i is the unknown vector at the i -th node, \vec{n} is the normal to the cell boundary and \mathcal{R} is the Roe Matrix. The matrix $P(W_i, W_j)$ is the Turkel-type preconditioning term, introduced to avoid accuracy problems at low Mach numbers. According to [11], we use this preconditioning only in the stabilizing terms and time consistency is preserved. Finally, the parameter γ_s multiplies the upwind part of the scheme and permits a direct control of the numerical viscosity, leading to a full upwind scheme (the usual Roe scheme) for $\gamma_s = 1$ and to a centered scheme when $\gamma_s = 0$.

The spatial accuracy of quadrature (41) is only first order. Two reconstruction steps are allied for increasing the accuracy. First, the MUSCL linear reconstruction method (“Monotone Upwind Schemes for Conservation Laws”), introduced by Van Leer [18], is adapted. The basic idea is to express the Roe flux as a function of a reconstructed value of W at the boundary between the two cells centered respectively at nodes i and j : $\Phi^R(W_{ij}, W_{ji}, \vec{n}_{ij})$. W_{ij} and W_{ji} are extrapolated from the values of W at the nodes, as follows:

$$W_{ij} = W_i + \frac{1}{2} \left(\vec{\nabla} W \right)_{ij} \cdot \vec{i}j \quad (42)$$

$$W_{ji} = W_j - \frac{1}{2} \left(\vec{\nabla} W \right)_{ji} \cdot \vec{i}j \quad (43)$$

Schemes with different properties can be obtained by different numerical evaluation of the slopes $\left(\vec{\nabla} W \right)_{ij} \cdot \vec{i}j$ and $\left(\vec{\nabla} W \right)_{ji} \cdot \vec{i}j$. In a second step, the slopes are defined in a parametrized form:

$$\begin{aligned} \left(\vec{\nabla} W \right)_{ij} \cdot \vec{i}j &= (1 - \beta) \left(\vec{\nabla} W \right)_{ij}^C \cdot \vec{i}j + \beta \left(\vec{\nabla} W \right)_{ij}^U \cdot \vec{i}j \\ &+ \xi_c \left[\left(\vec{\nabla} W \right)_{ij}^U \cdot \vec{i}j - 2 \left(\vec{\nabla} W \right)_{ij}^C \cdot \vec{i}j + \left(\vec{\nabla} W \right)_{ij}^D \cdot \vec{i}j \right] \\ &+ \xi_d \left[\left(\vec{\nabla} W \right)_M \cdot \vec{i}j - 2 \left(\vec{\nabla} W \right)_i \cdot \vec{i}j + \left(\vec{\nabla} W \right)_j \cdot \vec{i}j \right] \end{aligned} \quad (44)$$

$\left(\vec{\nabla} W \right)_{ij}^U$ is the gradient on the upwind tetrahedron T_{ij} , $\left(\vec{\nabla} W \right)_{ij}^D$ is the gradient on the downwind tetrahedron T_{ji} , $\left(\vec{\nabla} W \right)_i$ is the nodal gradient computed over the finite-volume cell around node i , $\left(\vec{\nabla} W \right)_j$ is the nodal gradient computed over the finite-volume cell around node j , $\left(\vec{\nabla} W \right)_{ij}^C$ is the centered gradient ($\left(\vec{\nabla} W \right)_{ij}^C \cdot \vec{i}j = W_j - W_i$) and $\left(\vec{\nabla} W \right)_M$ is the gradient at the point M . This last gradient is computed by interpolation of the nodal gradient values at the nodes contained in the face opposite to i in the upwind tetrahedron T_{ij} . The reconstruction of W_{ji} is analogous.

In choosing a particular set of free coefficients (β , ξ_c , ξ_d) in Eq. (44) attention has been dedicated to the dissipative properties of the resulting scheme which is a key point for its successful use in LES simulations. Two schemes have been proposed: the first one (V4) [27] is characterized by $\beta = 1/3$, $\xi_c = \xi_d = 0$, while the latter (V6) [26] is obtained by $\beta = \frac{1}{3}$, $\xi_c = -\frac{1}{30}$ and $\xi_d = -\frac{2}{15}$. The numerical dissipation in the schemes V4 and V6 is made of fourth- and sixth-order space derivatives,

respectively, and, thus, it is concentrated on a narrow-band of the highest resolved frequencies. As previously stated, this is important in LES simulations to limit as far as possible the interactions between numerical and SGS dissipation, which could deteriorate the accuracy of the results. The V6 scheme is used in the simulations reported herein.

Time advancing is carried out through an implicit linearized method, based on a second-order accurate backward difference scheme and on a first-order approximation of the Jacobian matrix [21]. The resulting numerical discretization is second-order accurate both in time and space.

5 Hybrid computation of supercritical flow

The application of a hybrid formulation to the simulation of the flow around bluff bodies at high Reynolds numbers of the order of millions is a difficult task because of the thin boundary layer to capture. Indeed, with the Reynolds number increasing, the boundary layer becomes turbulent and the angle of separation increases. This section is devoted to a first application of our hybrid model to this class of applications. As explained in the introduction of this chapter, in order to improve the industrial efficiency for high Reynolds flow, we investigate the possibility to exploit as much as possible the wall law and to use very coarse meshes. One of the consequences in using coarse grids is that van Kármán instabilities cannot be well captured, but using fine grids is almost unreachable because of computational costs, thus a compromise has to be found.

Our benchmark test is the flow around a circular cylinder for Reynolds numbers ranging between $500K$ and $3M$.

As least after the work of Roshko in 1961 [25] and Achenbach in 1968 (voir ref de 68) the aerodynamic loads on a circular cylinder in a cross-flow are known as highly sensitive to the value of Reynolds number, but only a few investigations have been realised for Reynolds number more than $5 \cdot 10^6$. This interval is inside the supercritical regime appearing for Reynolds number more than $200K - 300K$ for which the separation becomes turbulent. It is generally accepted that periodic vortex sheddings is very weak (if any) in the lowest parts of the interval. The range $0.48 \cdot 10^6$ to $7 \cdot 10^6$ has been measured by van Nunen in 1972. At the lower value $0.48 \cdot 10^6$ a fairly late turbulent separation is observed. With increasing Reynolds number the final separation point moves forward. This corresponds to a slight increase of the drag.

According to Jones [14] the interval $1.1 \cdot 10^6 < Rey < 3.5 \cdot 10^2$ is categorised into the wide-band random regime. Van Nunen suggests that a better range for this regime is 0.5-2.5, in that regime essentially no periodicity is observed for the unsteady lift or the unsteady pressures.

The narrow-band random regime corresponds to: $2.5 - 6.5 \cdot 10^6$. In this regime a small peak could be observed in the unsteady lift frequency analysis at Strouhal $St = 0.20$. This peak frequency applies at the front part of the cylinder and not beyond the separation point.

Measurements of these flows can be found in [25, 1, 35]. Besides these authors measurements of these flows can be found in [30, 31, 37, 39].

These flows have been computed by a few authors. Travin *et al.* use the Detached Eddy Simulation (DES) method [34, 36] on a mesh of about $400K$. They obtained pressures that are "consistently lower than in the majority of the experiments".

Catalano *et al.* [36] have used the combination of the LES with a wall model on a mesh of $2.3M$ nodes and could not predict good sensitivities to Reynolds numbers.

The geometrical structure of our computational domain is the same as in Figure ???. Periodic boundary conditions are applied in the spanwise direction while no-slip conditions are imposed on the cylinder surface. Characteristic based conditions are used at the inflow and outflow as well as on the lateral surfaces. The freestream Mach number is set equal to 0.1 in order to make a sensible comparison with incompressible simulations in the literature. Preconditioning is used to deal with the low Mach number regime. The computational domain is discretized by unstructured grid consisting

of approximately 274K nodes.

The simulation is performed using our hybrid RANS/VMS-LES model with dynamical SGS closure. The treatment of the boundary layer has received much attention, in our case we capture it with the statistical model, RANS with $k - \epsilon$ closure model and wall treatment with wall law as explained in Section 3.2. A schematic illustration of the boundary layer with wall law treatment is done in Figure 1, where:

- $\delta_{matching}$ is the thickness of the wall law zone, and we shall denote y_{match}^+ the normalized distance y to the wall: $y_{match}^+ = \frac{\delta_{match} U_f}{\gamma}$
- y_{mesh}^+ is the normalized size of the first layer of the mesh : $y_{mesh}^+ = \frac{\Delta x U_f}{\gamma}$ whereThe value of the friction velocity U_f is a priori chosen within the empirical law: $U_f = 1/20$???

As regards the blending function, the protection zone is used, with the blending function defined as in Relation (38) to avoid a mismatch near the wall. Figure 3 illustrates the blending function behavior for this benchmark at Reynolds number 1M and 3M. We observe with red color the RANS flow and in blue LES. The near wall region it is indeed treated with RANS, and this layer diminishes with Reynolds number increasing. We observe also additional fluctuations at higher Reynolds number, both in the near wall and respectively wake regions. As expected, the detachment angle increases with Reynolds number and this is well captured by the blending function too.

Computations are performed with our parallel MPI in-house solver AIRONUM written in Fortran 95 using 64 processors in this particular case.

Several issues are adressed for this benchmark.

5.1 Maximum mixing length in the dynamical model

Firstly, regarding our dynamic SGS Smagorinsky model. In Figure 5 the effect of $(C_s \Delta_{max})^2$ parameter was analysed. We recall that C_s is the Smagorinski constant and Δ is the size of the filter. The quantity $(C_s \Delta_{max})^2$ is interpreted as the maximum "mixing length". More precisely, we analyse the sensitivity of the computation to this filter component, usually in the litterature users allow for hundred times greater values than for the non-dynamic model. In our case according to our simulation shown in Figure 5 when this parameter is twice compared to the size of the non-dynamic, *i.e.*

$$C_s \Delta_{max} = 2 * C_s \Delta$$

then it tends to be too dissipative. In contrast, when we set it as the size of the non-dynamic:

$$C_s \Delta_{max} = C_s \Delta$$

we can say that it is a very reasonable compromise. Therefore, we choose this latest value for our simulations.

In Fluid Dynamics, drag crisis is a phenomenon in which drag coefficient drops off suddenly as Reynolds number increases. This corresponds to the point where the flow pattern changes, leaving a narrower turbulent wake. Drag and lift oscillations are captured for several Reynolds numbers: 1M (Figure 7), 1.5M (Figure 8) for our dynamical hybrid model. We can observe on this two figures that the mean drag, and thus lift, is growing with Reynolds number, which is the behaviour we expect for supercritical flows following the drag crisis curve.

Since the grid we are using is quite coarse, of about 274K cells (see snapshot in Figure 2) it becomes reasonable to compare the hybrid computation with the statistical RANS one. On Figures 9 and 10 we perform this comparaison for Reynolds numbers 2M and respectively 3M. We observe that at such high Reynolds numbers, on the contrary to what we are used, the RANS flow have a very irregular behaviour, and at Reynolds=3M, the mean values are slightly growing in comparaison with the hybrid model (see also Table 1).

5.2 Wall mesh size

Next, the effect of the grid is analysed for RANS model, more precisely, the sensitivity to the first mesh size y_{mesh}^+ . Firstly, the number of grid points was kept identical, we fixed the first mesh size and thus, the thickness of the wall law zone δ changes with Reynolds number. Next, we compared this series of simulations with the RANS simulation for fixed mesh for each Reynolds number. As it is illustrated in Figure 6 with Reynolds number increasing, RANS computation is more sensitive to fixed mesh, while for δ varying (becoming more and more narrow for fixed y_{match}^+) we are closer to experiments, but still not a perfect matching.

In Figure 11 we plot the drag coefficient at several supercritical Reynolds numbers for RANS and hybrid computations (using the same mesh) and compared with the experimental data. The simulation shows that starting from $Re = 5M$ our hybrid model still follows the experiments, while the RANS simulation gives a drag value above the normal one.

Next, the instantaneous vorticity is plotted in Figure 4 for hybrid computation at $Rey = 2M$ and $Rey = 3M$. Comparing these two results we notice that the wake is narrower at $Rey = 2M$ and the boundary separation slightly delayed than for $Rey = 3M$, resulting in a slightly smaller drag coefficient. Note that the thin boundary layer seen in this Figure is not representative, the true boundary layer with strong vorticity is extremely thin and not captured here.

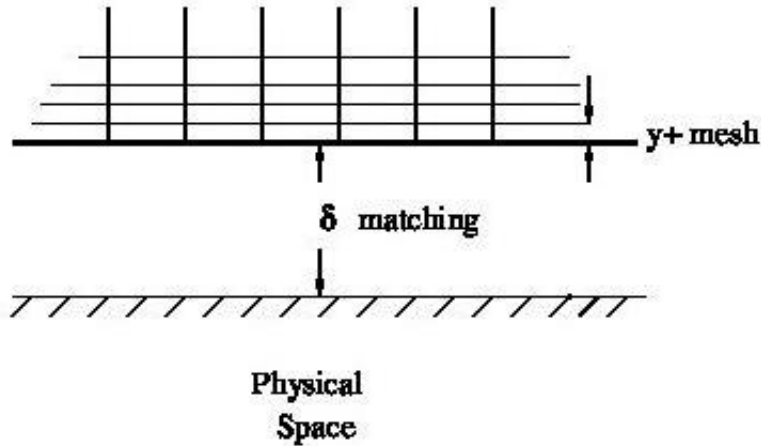


Figure 1: Sketch of the boundary treatment with wall law

Hybrid computations			
Rey	\bar{C}_d	C'_l	St
$1M$	0.24	0.020	0.073
$1.5M$	0.30	0.034	1.248
$2M$	0.35	0.048	0.443
$3M$	0.44	0.063	3.77

RANS computations		
Rey	\bar{C}_d	C'_l
$2M$	0.35	0.030
$3M$	0.49	0.067

Table 1: Bulk flow parameters predicted by our dynamic Hybrid RANS/VMS-LES model (table on the left) and RANS model (table on the right): Rey is the Reynolds number, \bar{C}_d is the mean drag, C'_l is the root mean square (r.m.s) of the lift coefficient, St is the Strouhal number associated with vortex shedding.

year = 1969

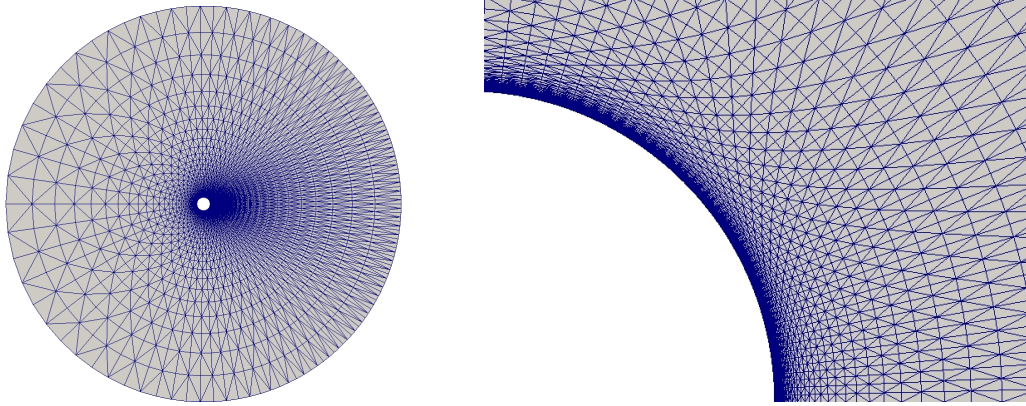


Figure 2: Snapshot of the surface mesh for Reynolds number $1M$, with $274K$ cells, $y+_{match} = 100$ and $y+_{mesh} = 10$; zoom on the near-wall mesh (image on the right).

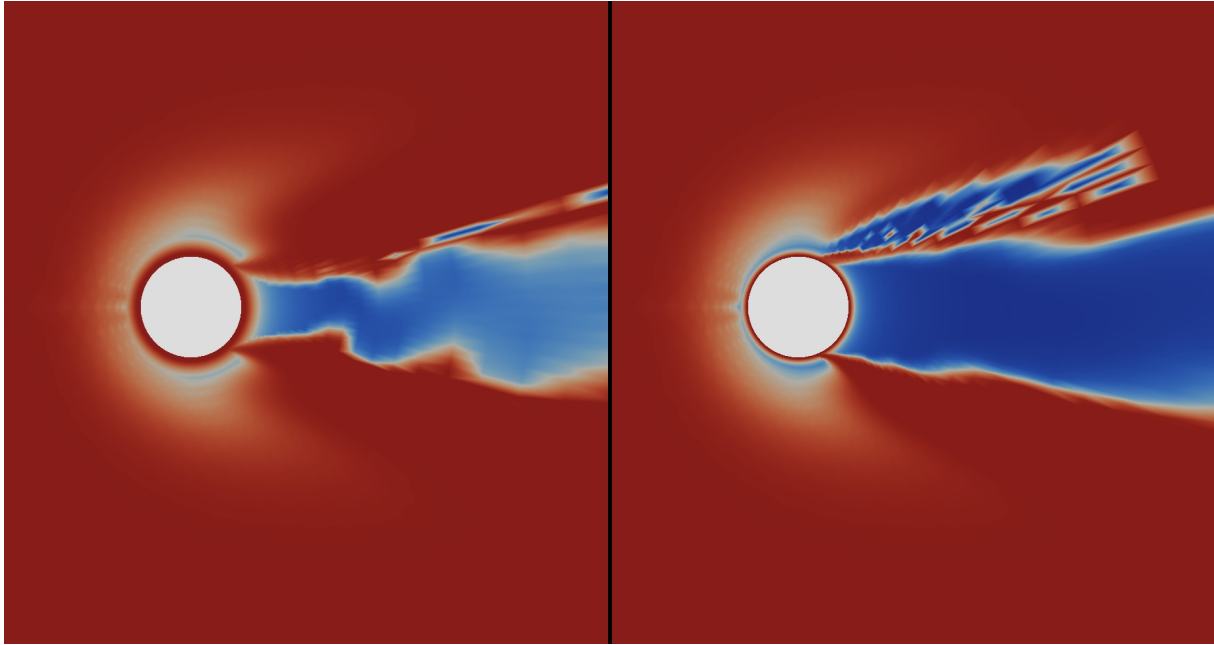


Figure 3: Hybrid computation: Visualisation of the blending function for Reynolds number $1M$ (left image) vs $3M$ (image on the right).

5.3 Conclusion

Our turbulence models discussed in this chapter are dealing with automatic variation of the viscous coefficients not only in spatial direction thanks to the dynamical model, but also in the sens of fluctuation scales thanks to the VMS formulation. The simulations performed with our hybrid model shows a rather good agreement with experimental data for coarse meshes. Further investigation on the sensitivity of the computation to $y+_{mesh}^+$, maybe an improved theoretical law defining a relation between the size of the matching zone and $y+_{mesh}^+$ for supercritical flows can be consider in the future.

year = 1969

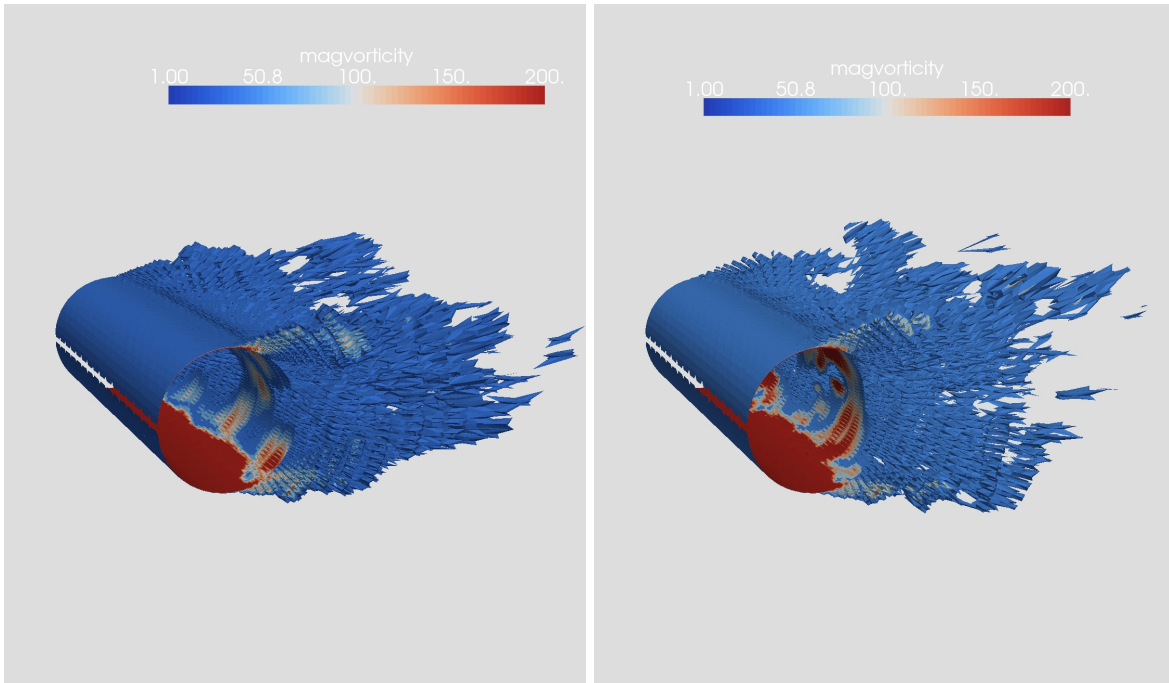


Figure 4: Hybrid computation: Visualisation of the vorticity for Reynolds number $2M$ (image on the left) vs $3M$ (image on the right).

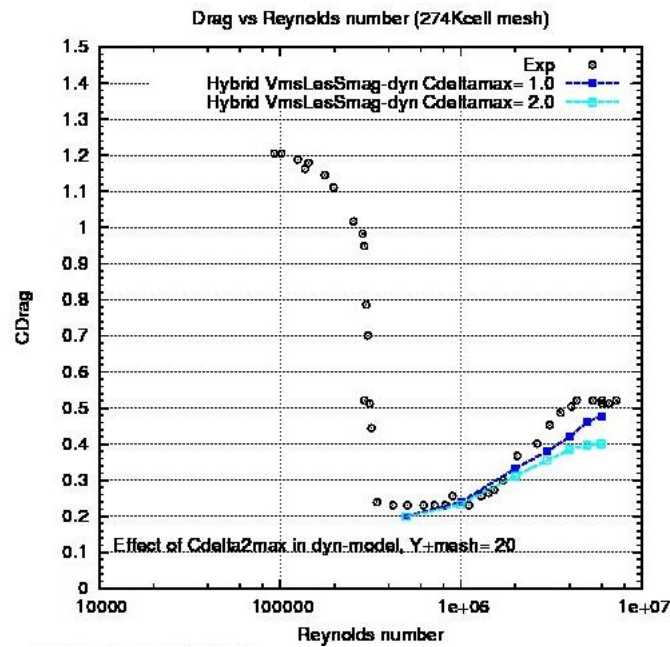


Figure 5: Effect of $C\Delta_{max}$ on our dynamic hybrid RANS/VMS-LES model for Reynolds numbers ranging from $500K$ to $8M$, comparison with experiments [30]

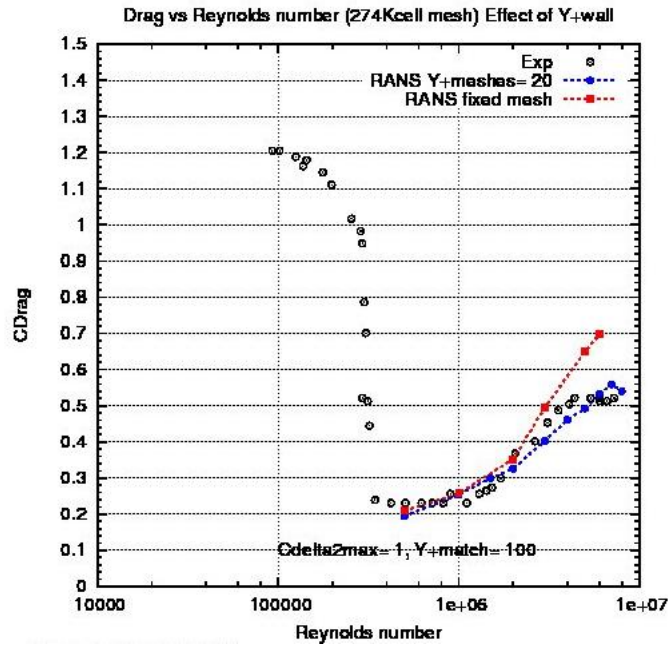


Figure 6: Analysis of the effect of first mesh size on RANS computations for y_{mesh}^+ fixed (thus, the thickness of the wall law zone $\delta_{matching}$ varying with the Reynolds number) and RANS computation with fixed mesh for each Reynolds number.

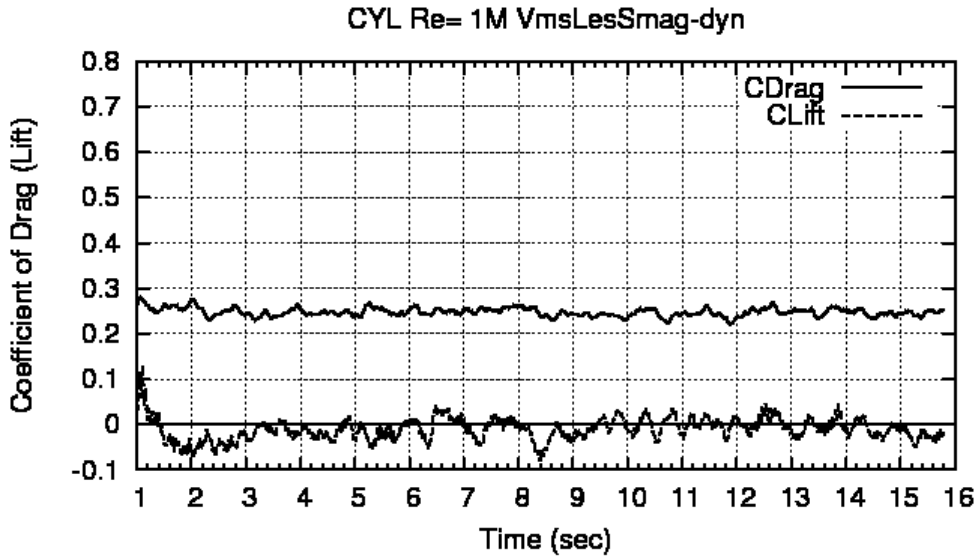


Figure 7: Flow over a circular cylinder at Reynolds number $1M$: Time-dependent forces. Upper curve: drag C_d , lower curve: lift C_l .

6 Concluding remarks

A variational multiscale LES approach combined with dynamic SGS models have been presented and used for the simulation of bluff body flows in subcritical regime. More specifically, the simulation

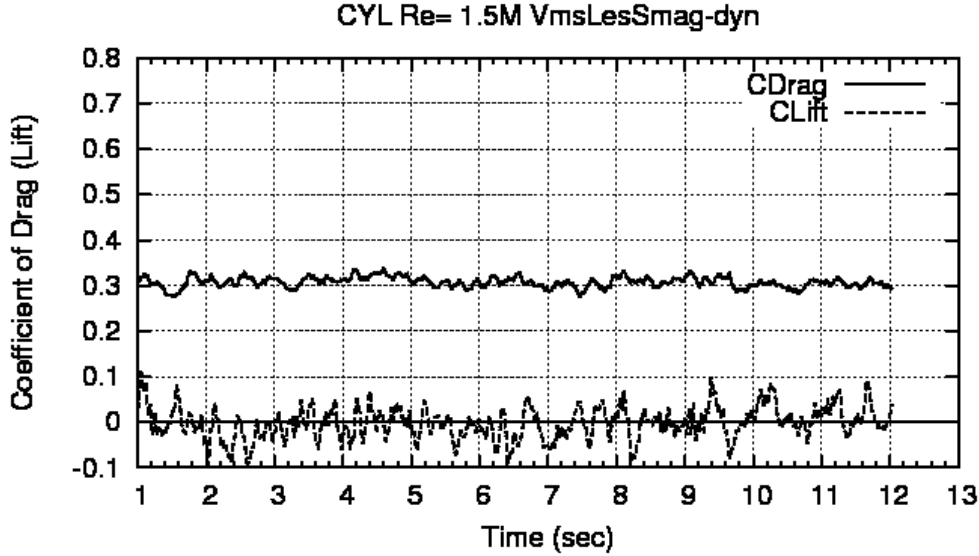


Figure 8: Flow over a circular cylinder at Reynolds number $1.5M$: Time-dependent forces. Upper curve: drag C_d , lower curve: lift C_l .

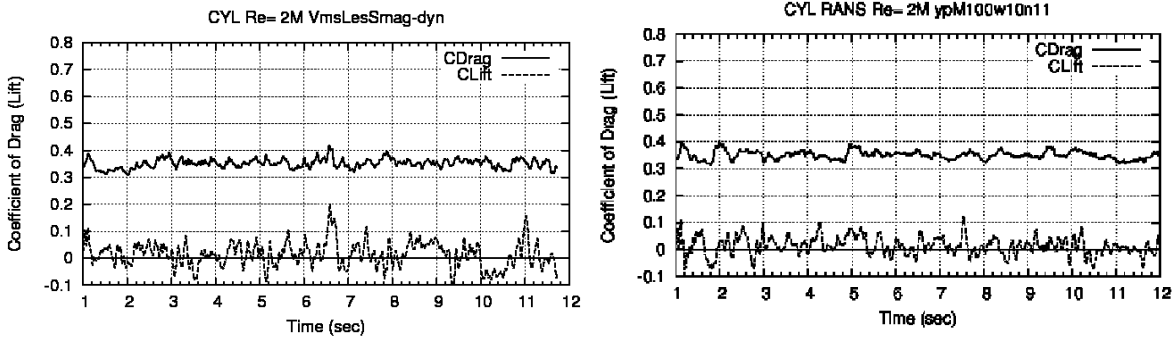


Figure 9: Flow over a circular cylinder at Reynolds number $2M$: Time-dependent forces. Upper curve: drag C_d , lower curve: lift C_l . Comparison between dynamic hybrid RANS/VMS-LES model (left image) with RANS (right image)

of the flow around a cylinder at $Re = 20000$, and the flow around a sphere at $Re = 10000$ and $Re = 50000$ have been carried out. The key ingredients of the used numerics and modeling are : unstructured grids, a second-order accurate numerical scheme stabilized by a tunable numerical diffusion proportional to sixth-order space derivatives, and the VMS-LES approach combined with the dynamic version of Smagorinsky and WALE SGS models. The overall results show the capabilities of the proposed dynamic VMS-LES model to accurately predict the aerodynamic forces acting on the considered bluff bodies, and to properly capture the main flow features associated to such vortex shedding flow problems. year = 1969

The hybrid turbulence models discussed in this paper are dealing with automatic variation of the viscous coefficients not only in spatial direction thanks to the dynamical model, but also in the sens of fluctuation scales thanks to the VMS formulation. The simulations performed with our hybrid model shows a rather good agreement with experimental data for coarse meshes. Further investigation on the sensitivity of the computation to y_{mesh}^+ , maybe an improved theoretical law defining a relation

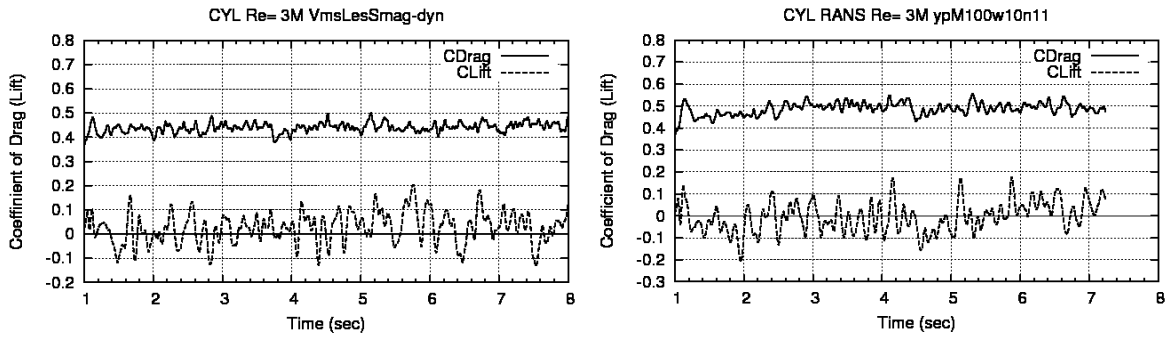


Figure 10: Flow over a circular cylinder at Reynolds number $3M$: Time-dependent forces. Upper curve: drag C_d , lower curve: lift C_l . Comparison between dynamic hybrid RANS/VMS-LES model (left image) with RANS (right image)

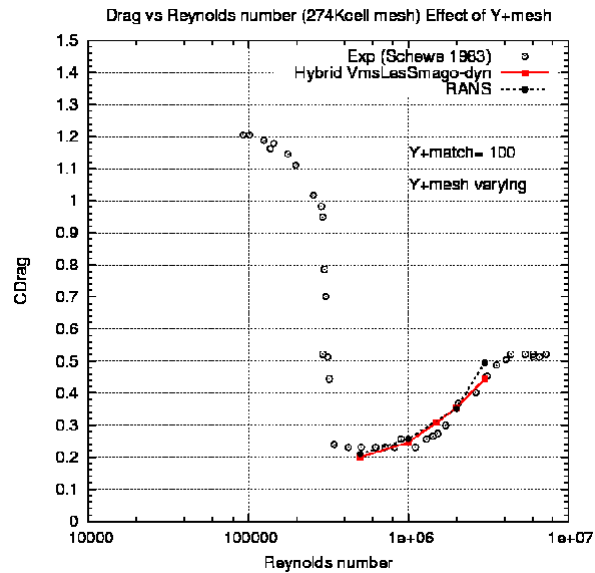


Figure 11: Drag vs. Reynolds curve: Comparing RANS and Hybrid computations with Experimental data of [30].

between the size of the matching zone and y_{mesh}^+ for supercritical flows can be consider in the future.

7 Acknowledgements

This work has been supported by French National Research Agency (ANR) through COSINUS program (project ECINADS n° ANR-09-COSI-003). HPC resources from GENCI-[CINES] (Grant 2010-x2010026386 and 2010-c2009025067) are also gratefully acknowledged.

References

- [1] E. Achenbach. Distribution of local pressure and skin friction around a circular cylinder in cross-flow up to $re = 5 \cdot 10^6$. *J. Fluid Mech*, 34(4):625–639, 1968.

Simulations	mesh size	\bar{C}_d	C'_l	Cp_{base}	θ	St
Hybrid RANS/VMS-LES	274K	0.24	0.020	0.30	117	
Hybrid RANS/VMS-LES dynamic	274K	0.24	0.020	0.30	117	
Hybrid RANS/VMS-LES	1.8M	0.24	0.020	0.30	117	
Hybrid RANS/VMS-LES dynamic	1.8M	0.24	0.020	0.30	117	
RANS		0.25	0.026	0.34	119	
LES of Kim and Mohan [15]		0.27		0.12	0.28	
LES of Wang et al. [36]		0.31		0.32		
LES of Catalano et al. [4]		0.31		0.32		0.35
Experiments						
Shih et al. [31]		0.20		0.33		
Schewe [30]		0.22				
Zdravkovich [39]		0.25				

Table 2: Bulk flow parameters prediction for simulations at $Rey = 1M$: \bar{C}_d is the mean drag, C'_l is the root mean square (r.m.s) of the lift coefficient, θ is the separation angle. Comparison with experimental data of [31, 39].

Simulations	\bar{C}_d	C'_l	Cp_{back}	θ
Hybrid RANS/VMS-LES dynamic	0.30	0.034	0.36	116
RANS	0.31	0.044	0.38	124
Experiments				
Schewe [30]	0.22			

Table 3: Bulk flow parameters prediction for simulations at $Rey = 1.5M$: \bar{C}_d is the mean drag, C'_l is the root mean square (r.m.s) of the lift coefficient, θ is the separation angle.

- [2] N. Botterill, H. Morvan, and J. Owen. Investigation into numerical modelling of the drag crisis for circular cylinders. In *Proceedings of BBAA VI International Colloquium on: Bluff Bodies Aerodynamics and Applications*, 2008.
- [3] B. Koobus C. Farhat and H. Tran. Simulation of vortex shedding dominated flows past rigid and flexible structures computational methods for fluid-structure interaction 1–30. tapir 1999.
- [4] P. Catalano, M. Wang, G. Iaccarino, and P. Moin. Numerical simulation of the flow around a circular cylinder at high reynolds numbers. *Int. J. Heat and Fluid Flow*, 24:463–469, 2003.
- [5] DES comput.
- [6] LES comput.
- [7] RANS comput.
- [8] comput with different Re.
- [9] U. Goldberg and D. Ota. A $k - \varepsilon$ near-wall formulation for separated flows. Technical Report 91–1482, AIAA 22nd Fluid Dynamics, Plasma Dynamics & Lasers Conference, June 1990.
- [10] U. Goldberg, O. Peroomian, and S. Chakravarthy. A wall-distance-free $k - \varepsilon$ model with enhanced near-wall treatment. *Journal of Fluids Engineering*, 120:457–462, 1998.
- [11] H.Guillard and C. Viozat. On the behaviour of upwind schemes in the low mach number limit. *computers and fluids* 28 :63-86, 1999.
- [12] J. Hinze. *Turbulence*. McGraw-Hill, 1959.
- [13] T.J.R. Hughes and M. Mallet. A new finite element formulations for computational fluid dynamics: Iii. *Comput. Methods Appl. Mech. Engrg.*, 58:329–336, 1986.

Simulations	\bar{C}_d	C'_l	$C_{p_{back}}$	θ
Hybrid RANS/VMS-LES dynamic	0.35	0.048	0.38	114
RANS	0.35	0.030	0.42	108
LES [36]	0.32	—	—	—
Experiments				
Schewe [30]				

Table 4: Bulk flow parameters prediction for simulations at $Rey = 2M$: \bar{C}_d is the mean drag, C'_l is the root mean square (r.m.s) of the lift coefficient, θ is the separation angle.

Simulations	\bar{C}_d	C'_l	$C_{p_{base}}$	θ
Hybrid RANS/VMS-LES dynamic	0.44	0.063	0.47	107
RANS	0.49	0.067	0.55	109
DES with rotation/curvature term [34]	0.51	0.10	0.64	106
DES without rotation/curvature term [34]	0.41	0.06	0.53	111
Experiments				
Nunen [35]	—	—	—	120

Table 5: Bulk flow parameters prediction for simulations at $Rey = 3M$: \bar{C}_d is the mean drag, C'_l is the root mean square (r.m.s) of the lift coefficient. comparison with experimental data of [35].

- [14] G.W. Jones, J. Cincotta, and R.W. Walker. Research Report R-300, NASA, 1969.
- [15] S.-E. Kim and L.S. Mohan. Prediction of unsteady loading on a circular cylinder in high reynolds number flows using large eddy simulation. *Proceedings of OMAE 2005: 24th International Conference on Offshore Mechanics and Artic Engineering, june 12-16, Halkidiki, Greece, OMAE 2005-67044*, 2005.
- [16] B. Koobus and C. Farhat. A variational multiscale method for the large eddy simulation of compressible turbulent flows on unstructured meshes-application to vortex shedding comput. *methods appl. mech. eng.* 193 :1367-1383 2004.
- [17] B.E. Launder and D.B. Spalding. The numerical computation of turbulent flows. *Comp. Meth. Appl. Mech. and Eng.*, 3:269–289, 1979.
- [18] B. Van. Leer. Towards the ultimate conservative scheme. iv :a new approach to numerical convection. *j. comp. phys.* 23 :276-299, 1977.
- [19] D. K. Lilly. A proposed modification of the germano subgrid scale closure model physics of fluids a 4 633 1992.
- [20] P. Moin W.H. Cabot M. Germano, U. Piomelli. A dynamic subgrid-scale eddy viscosity model, physics of fluids, a 3 1760-1765 1991.
- [21] R. Martin and H.Guillard. A second-order defect correction scheme for unsteady problems comput. and fluids, 25(1) :9-27, 1996.
- [22] H. Steve M.H. Lallemand and A. Dervieux. Unstructured multigriding by volume agglomeration : current status comput. fluids 21 397-433 1992.
- [23] F. Nicoud and F. Ducros. Subgrid-scale stress modellinng based on the square of the velocity gradient tensor flow turb. comb., 62(3) :183-200, 1999.
- [24] P.L. Roe. Approximate riemann solvers, parameters, vectors and difference schemes *j. comp. phys.* 43 :357-371, 1981.
- [25] A. Roshko. Experiments on the flow past a circular cylinder at very high reynolds numbers. *J. Fluid Mech.*, 10-3:345–356, 1961.

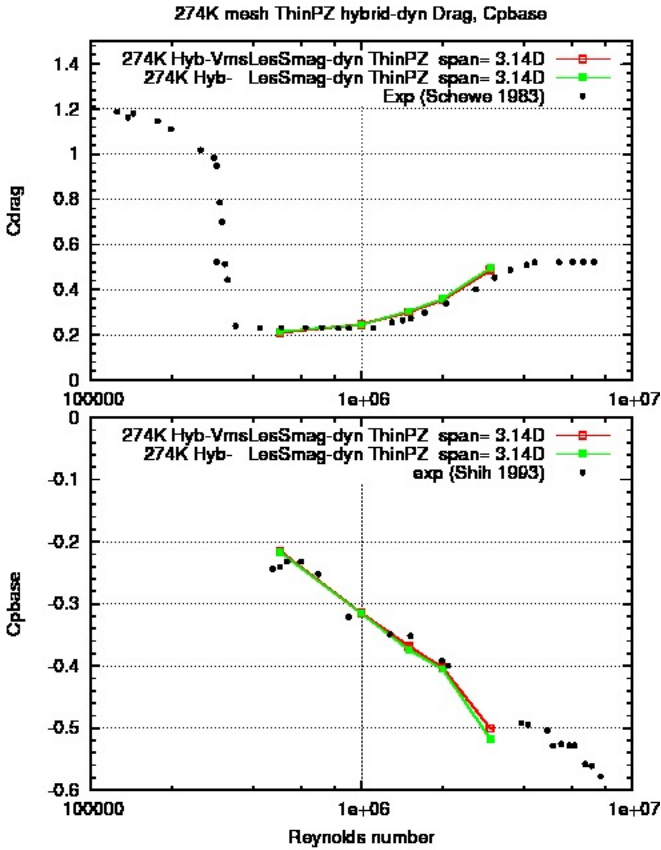


Figure 12: Strouhal vs. Reynolds curve: Comparing with Experimental data of [30].

- [26] B. Koobus S. Camarri, M. V. Salvetti and A. Dervieux. A low diffusion muscl scheme for les on unstructured grids comp. fluids 33 1101–1129 2004.
- [27] B. Koobus S. Camarri, M.V. Salvetti and A. Dervieux. Large-eddy simulation of a bluff-body flow on unstructured grids. int. j. num. meth. fluids, 40:1431–1460, 2002.
- [28] P. Moin K. Akselvoll S. Ghosal, T. Lund. The dynamic localization model for large eddy simulation of turbulent flows j. fluid mech. 286 229-255.
- [29] P. Sagaut and E. Labourasse. Reconstruction of turbulent fluctuations using a hybrid rans/les approach. *J. Comp. Phys.*, 182:301–336, 2002.
- [30] G. Schewe. On the force fluctuations acting on a circular cylinder in crossflow from subcritical up to transcritical reynolds numbers. *J. of Fluid Mechanics*, 133:265–285, 1983.
- [31] W.C. L. Shih, C. Wang, D. Coles, and A. Roshko. Experiments on flow past rough circular cylinders at large reynolds numbers. *J. Wind Engg. and Industrial Aerodynamics*, 49:351–368, 1993.
- [32] B.M. Sumer and J. Fredsoe. *Hydrodynamics around cylindrical structures*. World Scientific, 2006.
- [33] P. Sagaut sur VMS.

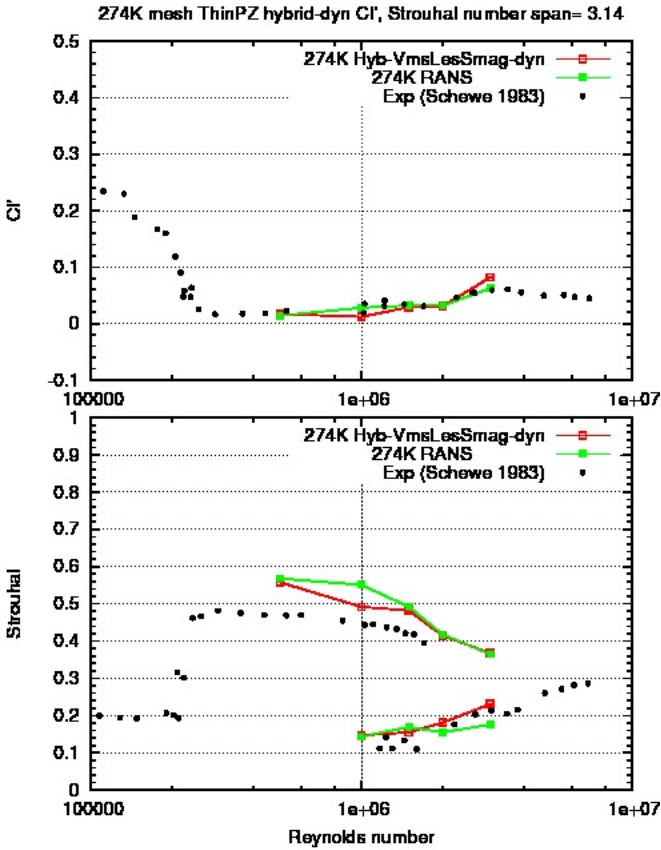


Figure 13: Strouhal vs. Reynolds curve: Comparing with Experimental data of [30].

- [34] A. Travin, M. Shur, M. Strelets, and P. Spalart. Detached-eddy simulations past a circular cylinder. *Flow, Turbulence and Combustion*, 63:293–313, 1999.
- [35] J.W.G. van Nunen. Pressure and forces on a circular cylinder in a cross flow at high reynolds numbers. In: *Naudascher, (Ed.) Flow Induced Structural Vibrations*, pages 748–754, 1974.
- [36] M. Wang, P. Catalano, and G. Iaccarino. Prediction of high reynolds number the flow over a circular cylinder using les. Annual research briefs, Center for Turbulence Research, Stanford, 2001.
- [37] K.A. Warschauer and J.A. Leene. Experiments on mean and fluctuating pressures of circular cylinders at cross-flow at very high reynolds numbers. In *Proc. Int. Conf. on Wind Effects on Buildings and Structures*, pages 305–315, Saiko, Tokyo, 1971.
- [38] V. Yakhot and S. A. Orszag. Renormalization group analysis of turbulence. i. basic theory. *Journal of Scientific Computing*, 1(1):3–51, 1986.
- [39] M.M. Zdravkovich. *Flow around circular cylinders Vol 1: Fundamentals*. Oxford University Press, 1997.

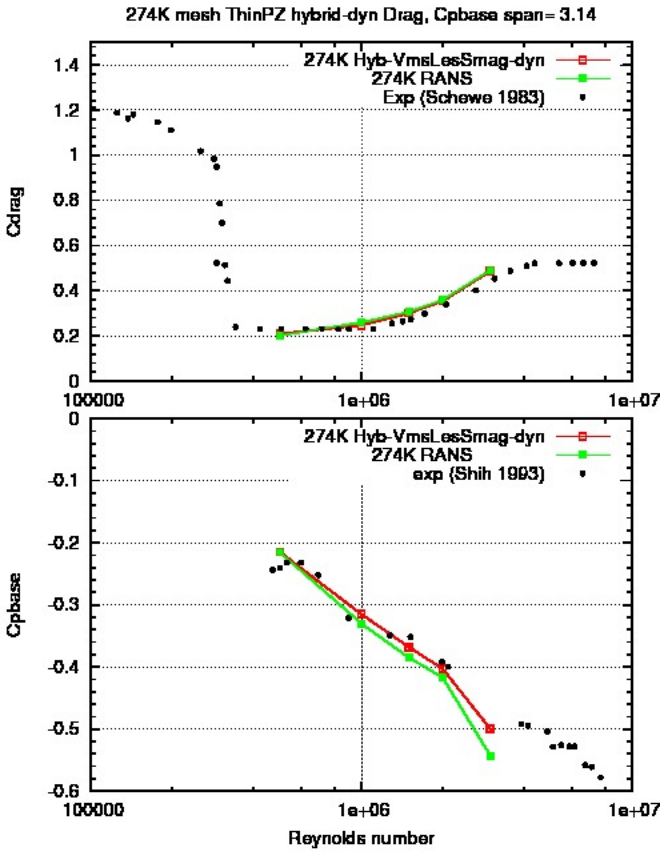


Figure 14: Strouhal vs. Reynolds curve: Comparing with Experimental data of [30].

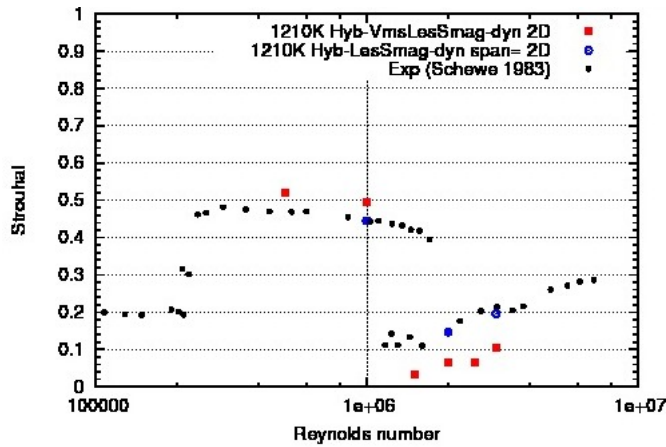


Figure 15: Strouhal vs. Reynolds curve: Comparing Hybrid-VMS and Hybrid-VMS-Dynamique computations with Experimental data of [30].

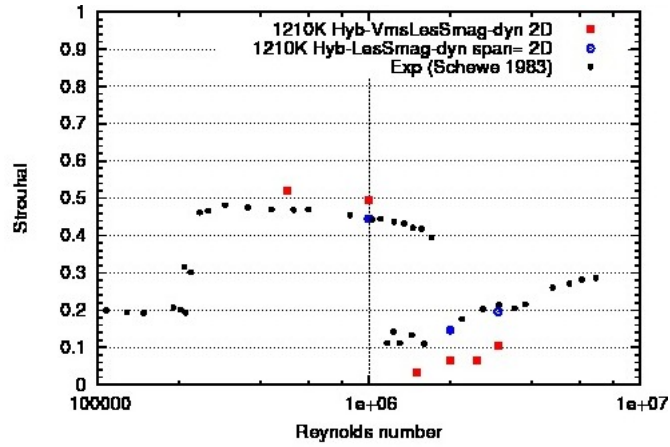


Figure 16: Strouhal vs. Reynolds curve: Comparing Hybrid-VMS and Hybrid-VMS-Dynamique computations with Experimental data of [30].

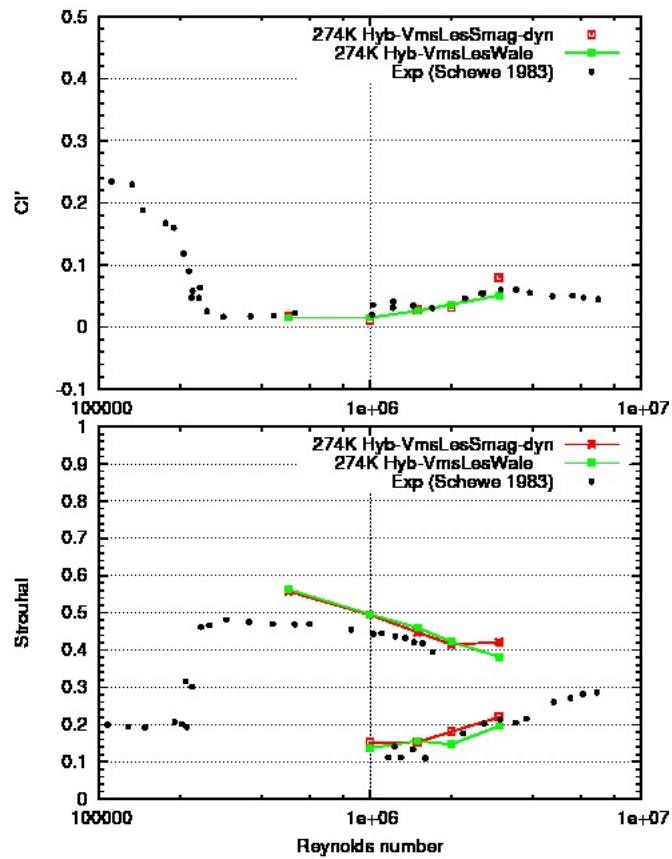


Figure 17: Strouhal vs. Reynolds curve: Comparing Hybrid-VMS Smagorinsky and WALE computations with Experimental data of [30].

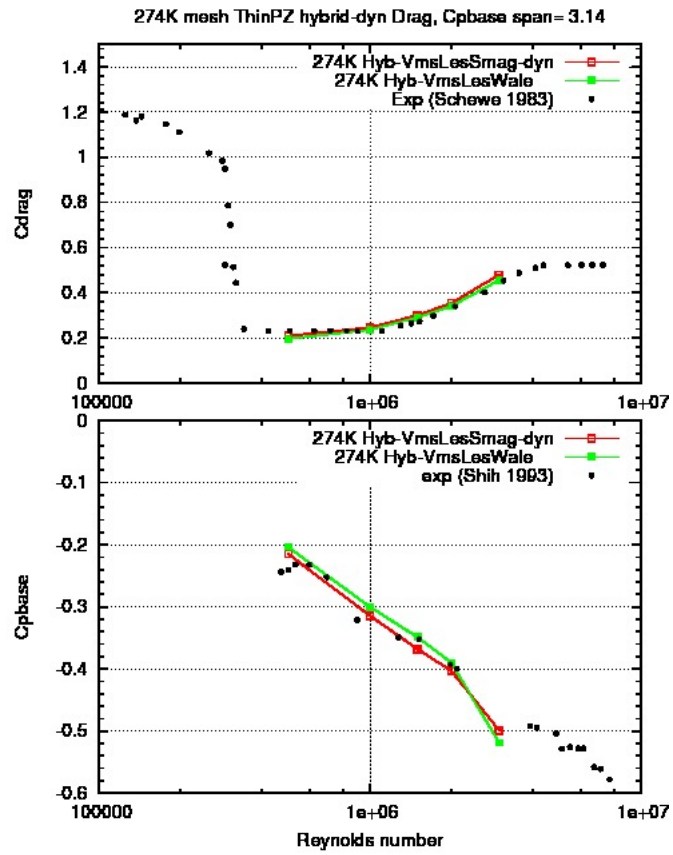


Figure 18: CPBase vs. Reynolds curve: Comparing Hybrid-VMS Smagorinsky and WALE computations with Experimental data of [30].

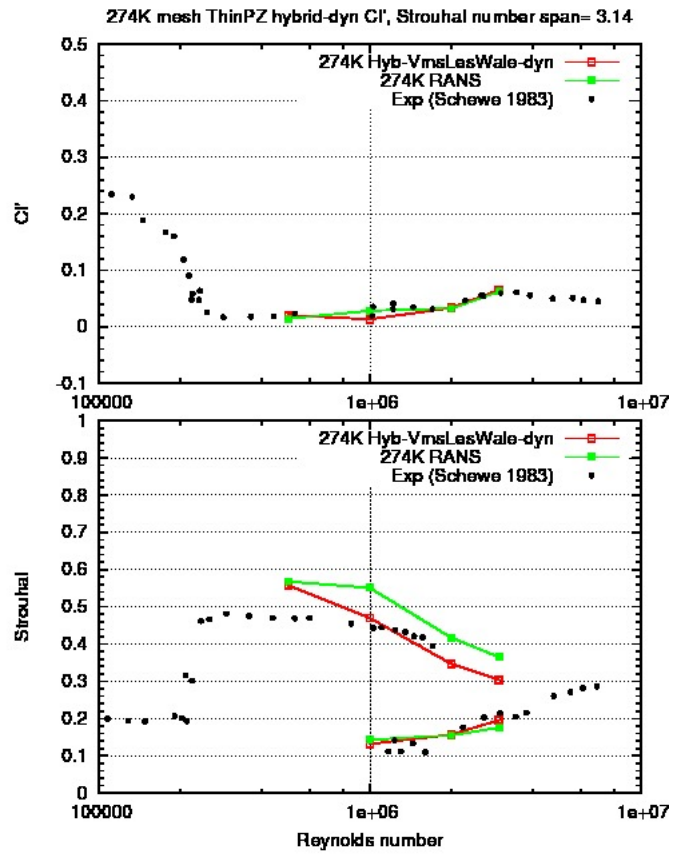


Figure 19: Strouhal vs. Reynolds curve: Comparing Hybrid-VMS WALE and RANS computations with Experimental data of [30].

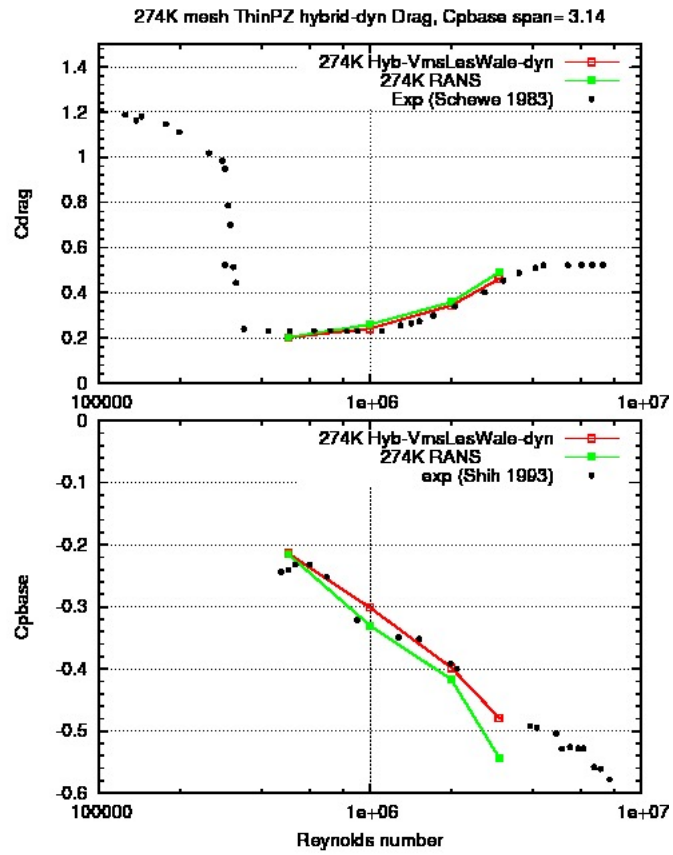


Figure 20: CPBase vs. Reynolds curve: Comparing Hybrid-VMS WALE and RANS computations with Experimental data of [30].